Tuning the interactions of a magnetic colloidal suspension

F. Cousin,[1,2] E. Dubois,[1] and V. Cabuil[1]

[1]*Laboratoire des Liquides Ioniques et Interfaces Chargées, CNRS UMR 7612, case 63, Université Pierre et Marie Curie,
4 Place Jussieu, 75252 Paris Cedex 05, France*
[2]*Laboratoire Léon Brillouin, CEA-CNRS, CEA Saclay, 91191 Gif sur Yvette, France*

We present a versatile experimental system of magnetic charged nanospheres dispersed in water that belongs to both dipolar and electrostatic systems. In this system, the interactions can be continuously tuned by varying the ionic strength I. At low I, the potential is a strongly repulsive Yukawa potential that leads to a phase diagram similar to the one of repulsive spheres (fluid and solid phases). At high I, the potential is a globally attractive Lennard-Jones potential that leads to a phase diagram similar to the one of atomic systems (gas, liquid, fluid, and solid phases).

PACS number(s): 83.80.Hj, 82.60.Qr, 64.30.+t, 75.50.Mm

INTRODUCTION

Contrary to atomic systems, suspensions of spherical colloids allow studying the phase behavior of assemblies of objects under various interparticle potentials because their shape can be easily changed experimentally [1].

For spherical colloids without anisotropic interactions, several theoretical studies predict that the phase behavior depends on the balance of attractive and repulsive interactions [2].

For repulsive systems, only fluid-solid transitions can be observed. For monodisperse systems, this transition is a Kirkwood-Alder fluid-crystal transition governed by entropy. It has been experimentally observed in electrostatic systems [3–5] and sterically stabilized hard spheres [6]. When the polydispersity of the system is too high, the solid phase is a glass [7].

For attractive systems, liquid-gas transitions can be observed depending on the range of the attractive part of the potential. Such transitions have been predicted in systems for which long-range attractions are induced by adjustable depletion interactions [8–10]. They have been observed both for sterically stabilized systems [11] and electrostatically stabilized systems [12–14]. Gas-liquid transitions have also been obtained in sterically stabilized systems by a change of the solvent quality [15–17]. On the contrary, they have been predicted for electrostatically stabilized systems [18] but never experimentally observed.

The influence of anisotropic interactions, as in dipolar fluids, has given rise to numerous theoretical studies on the phase behavior of dipolar systems [19–30], recently reviewed by Teixeira *et al.* [31].

One of the main question in these studies is the existence of gas-liquid transitions. In the past, it has been suggested that such transitions should appear in the presence of anisotropic dipolar interactions if the isotropic attractions are sufficiently strong. They are thus not observed in dipolar hard-spheres systems [19–22]. In dipolar Stockmayer fluids [23–26], in which dipolar interactions are weak, the phase behavior is close to that of atomic systems, i.e., gas-liquid transitions are allowed. If dipolar interactions are strong, the behavior is closer to pure dipolar fluids. This dipolar Stockmayer fluid is the most realistic description of a magnetic colloidal suspension as it takes into account van der Waals attractions.

Nevertheless, the debate on the phase behavior of dipolar fluids is still open as shown by recent studies [27–30]. New kinds of fluid-fluid transitions are predicted by simulations. The phases are no longer constituted of isolated particles but contain chains, the length of which depends on the particles density [28].

There is, nevertheless, a lack of experimental studies concerning both electrostatically stabilized colloids and real dipolar systems. We present in this paper a versatile experimental system of magnetic charged spheres in water that belongs to both dipolar and electrostatic systems. It provides experimental access to the range and strength of the interparticle potential for a wide variety of potential shapes by controlling a single parameter, the ionic strength. The phase behavior of the system is studied here without magnetic field, this step being essential prior to any study with an applied field.

We demonstrate here that the phase behavior observed can be separated into two regimes depending on the balance between the different interactions. The change in interaction regimes can be related to an inversion of the second virial coefficient A_2. When the potential is repulsive, only fluid-solid-like phase transitions (Fig. 1) are observed, whereas when the potential is attractive, the system exhibits the same phase diagram as an atomic system (Fig. 8).

I. INTERPARTICLE FORCES IN THE SYSTEM

The colloidal suspensions considered here are constituted of magnetic nanoparticles dispersed in water. The particles are coated with a citrate ligand, which gives them a negative charge at the pH of the study and thus ensures stabilization of the suspension by electrostatic repulsions. Theoretically, four kinds of forces contribute to the interparticle potential in the system, presented here by range order. However, their calculation poses several difficulties.

(i) At contact, there is a strong hard-core repulsion between the particles due to the steric hindrance between the citrate ligands adsorbed on the surface. The range of this
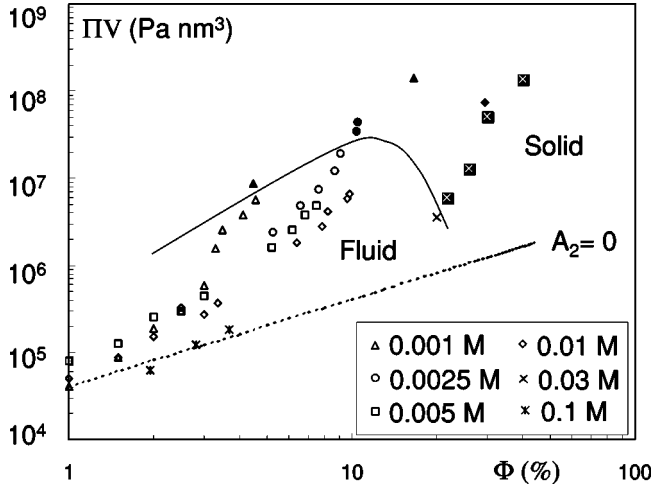
FIG. 1. Phase diagram at low ionic strength at $T = 293$ K, obtained with sample FF1. The open symbols represent the fluid samples and the filled ones the solid samples. The dashed line corresponds to $A_2 = 0$. The full line is a guide to the eye, which shows the limit between fluid and solid areas. $[\text{cit}]_{free}$ is given in the caption.

hard-core repulsion is of the order of two times the citrate size (~ 10 Å).

(ii) Van der Waals forces induce strong short-range isotropic attractions varying as $-1/r^6$, where r is the interparticle distance. For the calculation of the interparticle potential presented in the paper, we have used the following potential for the spheres of radius R [1]:

$$\frac{U_{VDW}(r)}{kT} = -\frac{A}{6kT}\left[\frac{R^2}{r^2 - 4R^2} + \frac{2R^2}{r^2} + \ln\left(1 - \frac{4R^2}{r^2}\right)\right],$$

where A is the Hamaker constant. This constant depends on the dielectric permittivities of the maghemite, citrate, and solvent [32]. The presence of the citrate layer considerably lowers the value of the bare maghemite particle [33] and is estimated here to be 3×10^{-20} J.

(iii) Magnetic dipolar forces between two particles induce anisotropic interactions, which are found to be globally attractive if the anisotropic interparticle potential describing such suspensions is integrated over all directions. These forces vary from $-1/r^6$ to $-1/r^3$ depending on the strength of the magnetic coupling $\gamma = (\mu_0/kT)(\mu_1\mu_2/r^3)$ between two particles of respective momentum μ_1 and μ_2 and thus are strongly size dependent.

For low values of γ ($\gamma/4\pi \ll 1$, low coupling regime), the dipoles rotate freely, the mean interaction is isotropic and the potential varies as $-1/r^6$, such as van der Waals attractions:

$$\left\langle \frac{U_{dip}}{kT}\right\rangle = -\frac{\gamma^2}{48\pi^2}.$$

For high values of γ ($\gamma/4\pi \gg 1$, high coupling regime), the interaction becomes anisotropic and has a longer range, as it varies as $-1/r^3$:

$$\left\langle \frac{U_{dip}}{kT}\right\rangle = -\frac{\gamma}{2\pi}.$$

The estimation of these magnetic dipolar interactions in our systems implies knowing γ, parameter which can only be determined precisely from experimental measurements [34]. The parameter $\gamma/4\pi$ is close to 1 and the dipolar interaction thus lies between the two limits described above.

(iv) Finally, the Coulomb forces introduce long-range electrostatic repulsions varying as $1/r^2$, which can be partially screened by adding salt into the suspension. The potential used in the calculation in this paper is a Yukawa potential coming from the Derjaguin-Landau-Verwey-Overbeek theory [35,36]:

$$\frac{U_{el}(r)}{kT} = \frac{Z_{eff}^2 L_B}{r}\frac{e^{-\kappa(r - 2R_{eff})}}{(1 + \kappa R_{eff})^2},$$

where $\kappa = [(e^2/\epsilon_0\epsilon kT)\Sigma_i c_i Z_i^2)^{1/2}]$ is the inverse of the Debye length. L_B is the Bjerrum length, R is the particle radius, Z_{eff} is the effective charge of a particle, R_{eff} is the effective radius of a particle, c_i is the concentration of the ionic specie i and Z_i its valency. Z_{eff} is an effective charge that takes into account the condensation of the counterions on the surface of the particles and can be estimated as $Z_{eff} = 4R/Z_C$, where Z_C is the valency of the counterion [37].

However, we shall show later on that the main difficulty is the evaluation of the range of the repulsion. It can be estimated from experimental data but cannot be easily calculated from simple models. Nevertheless, considering these four contributions, the interparticle potential calculated for the different regimes (Figs. 5, 7, and 12) is fully consistent with the experimental results.

II. EXPERIMENTAL SYSTEMS AND METHODS

The system is constituted of a dispersion of magnetic nanoparticles of maghemite γ-Fe$_2$O$_3$ in aqueous media [38]. The maghemite nanoparticles are chemically synthesized in water by coprecipitation of FeCl$_2$ and FeCl$_3$ in an alkaline solution [39]. The acidic properties of the surface of the particles obtained lead to a point of zero charge around 7 and thus, at low pH, to cationic particles. Their dispersion in water forms a stable colloidal suspension around pH 2. Since the diameter of the particles lie between 3 and 15 nm, corresponding to a wide size distribution, a size-sorting procedure is performed. It is based on the properties of the reversible phase transitions resulting from an electrolyte addition [40]. This reduces the polydispersity and allows varying the mean particle size.

Trisodium citrate molecules are then adsorbed on the surface of the particles and the pH is set to 7. The surface charge is negative, saturated at a value of 2 charges/nm^2, and neutralized by Na$^+$ counterions [38]. As the adsorbed citrate ions are in equilibrium with free citrate ions, the ionic strength I of the solution is due to the concentration $[\text{cit}]_{free}$ of the free citrate ions and the corresponding sodium counterions.

Each particle is a magnetic monodomain because the size of the particles is small enough to prevent the formation of Bloch walls. Thus, each particle bears a permanent magnetic moment $\mu = m_s V$, where m_s is the particle magnetization (3.1×10^5 A/m) and V is the particle volume. The suspensions thus present a giant paramagnetism. Their magnetization curve as a function of the applied magnetic field follows Langevin's law, on condition that the interactions are negligible, i.e., on condition that the solutions are sufficiently diluted. The strong dependence of the magnetization on the size of the particles allows determining the characteristics of the size distribution. This distribution is well described by a log normal law, characterized by a mean diameter d_0 ($\ln d_0 = \langle \ln d \rangle$) and a polydispersity σ, obtained from a two-parameter fit of the experimental curves measured at low volume fraction ($\Phi < 1\%$) [41].

All samples are prepared by osmotic compression [42], which allows to impose a chosen osmotic pressure Π and a chosen ionic strength I on a given suspension, in order to monitor interactions in the system. Experimentally, the colloidal suspension is dialyzed against a reservoir of known pressure and of known ionic strength. The reservoir fixes the chemical potential of water, and the osmotic pressure and ionic strength of the suspension. The volume fraction Φ is measured after equilibrium has been reached (typically after 2–3 week) from a chemical titration of iron. If the osmotic pressure is lower than 4000 Pa, it can also be measured with a membrane osmometer (Knauer ref A0330) between 10 and 4000 Pa with an accuracy of 5 Pa [43]. The membrane (cellulose 20 kDa) separates two compartments, one filled with the colloidal suspension and the other filled with a sodium citrate solution, the concentration of which equals $[\text{cit}]_{free}$ in the colloidal suspension. As a result, a solution is fully characterized by parameters Π, Φ, and I. We will therefore present the results in the Π-Φ plane that can be entirely explored using osmotic compression, following, for example, a line at constant Π or I.

SANS (small-angle neutron scattering) experiments are performed on the PAXY spectrometer (Orphée reactor, LLB, CEA, Saclay, France). Three different configurations of neutron wavelength λ and detector distance D are used: $\lambda = 10$ Å, $D = 3.1$ m; $\lambda = 5$ Å, $D = 3.1$ m; $\lambda = 5$ Å, $D = 1$ m. It leads to a global range of scattering vectors between 0.008 Å^{-1} and 0.4 Å^{-1}. For magnetic particles, the signal measured in SANS can come either from a nuclear contribution or from a magnetic contribution. Nevertheless, in the γ-Fe$_2$O$_3$ particles considered here, it has been shown in Ref. [34] that the intensity after subtraction of the incoherent background is largely dominated by the nuclear contribution of the particles when the measurement is performed in light water. SAXS (small-angle x-ray scattering) experiments are performed on the D22 spectrometer (Lure, Orsay, France). The wavelength is 1.24 Å, and the distance between the sample and the detector is 1.8 m, leading to scattering vectors from 0.007 Å^{-1} to 0.3 Å^{-1}.

In both cases, the form factor is determined from the intensity of noninteracting dilute particles, i.e., a volume fraction Φ_0 around 1%. The structure factor $S(q, \Phi)$ of concen-

TABLE I. Size characteristics of the samples.

Sample	d_0 (nm)	σ
FF1	7.5	0.35
FF2	6.15	0.18
FF3	6.9	0.14
FF4	7.3	0.21
FF5	8.8	0.2

trated suspensions is then deduced from the detected intensity $I(q, \Phi)$ using

$$S(q, \Phi) = \frac{[I(q, \Phi)/\Phi]}{[I(q, \Phi_0)/\Phi_0]}.$$

The different samples studied here are listed in Table I with their size characteristics deduced from magnetization measurements. Sample FF1 is the initial polydisperse sample. The other samples, issued from the size-sorting process carried out on sample FF1, have a reduced polydispersity and different mean sizes have been used depending on the regions explored in the phase diagram. Indeed, reducing polydispersity through fractionation reduces the volume of the suspension and exploring regions of high volume fractions necessitates large volumes of suspensions. A compromise between yield and monodispersity is thus necessary. Samples of different mean sizes lead to the same qualitative results but, as the pressure Π varies as $1/V$, the pressure needed to reach a given volume fraction is shifted with size; it is higher for monodisperse samples and for smaller particles. Therefore, the Π-Φ diagram will be replaced by a ΠV-Φ universal diagram: the volume used is the mean V_W determined from neutron scattering experiments [38].

III. LOW IONIC STRENGTH REGIME: REPULSIVE REGIME

A. Equation of state

When the ionic strength of the suspensions is low (typically $[\text{cit}]_{free} < 10^{-2}$ mol/L), the structure of the suspension is ruled by strong electrostatic repulsions. This can be seen on the equations of state at a given I plotted on a Π-Φ diagram (Fig. 1). Π can be described by a virial development

$$\frac{\Pi}{\Phi} = \frac{kT}{V}[1 + \rho^2 N_a V A_2 \Phi + 0(\Phi^2)],$$

where V is the volume of the particle, ρ is the density of the particle (g/cm^3), N_a is the Avogadro number, and A_2 is the second virial coefficient (mol g^{-2} cm^3). The situation $A_2 = 0$ corresponds to the perfect gas $\Pi \Phi = \rho kT$, and this line separates in the phase diagram the domains of the attractive and the repulsive interparticle potential. The experimental points for $[\text{cit}]_{free} < 0.03$ mol/L are far above this line, i.e., in the repulsive regime. The phase diagram also shows the data for $[\text{cit}]_{free} = 0.1$ mol/L, which are close to the line $A_2 = 0$. This indicates that this ionic strength borders on the

TABLE II. Range δ of the interaction extracted from osmotic pressure measurements and comparison to calculated values of the Debye length of a 3:1 electrolyte (sodium citrate) and of a 1:1 electrolyte with the same concentration as the 3:1.

$[cit]_{free}$ (mol/L)	10^{-3}	2.5×10^{-3}	5×10^{-3}	10^{-2}
δ (nm)	6.8	5.2	4.6	3.8
λ_{Debye} 3:1	4.0	2.5	1.8	1.25
λ_{Debye} 1:1	9.7	6.1	4.35	3.1

repulsive regime. In this region, only fluid and solid phases exist. The solid is defined according to a macroscopic observation; it does not flow under gravity.

For sufficiently low Φ values, the samples are fluid and the osmotic pressure increases dramatically with a decrease in ionic strength for a given volume fraction. This indicates a significant increase of the repulsion in the system. The experimental equations of state are accurately described by a Carnahan-Starling equation of state that gives the exact values for the virial coefficients up to A_4 for a hard-core potential, i.e., for hard spheres [44],

$$\frac{\Pi}{\Phi} = \frac{kT}{V} \frac{1 + \Phi + \Phi^2 - \Phi^3}{(1-\Phi)^3},$$

with an effective volume fraction Φ_{eff} that takes into account the range δ of the repulsion. Here, repulsions are indeed sufficiently strong for us to consider the particles as hard spheres with effective diameter equal to the sum of their diameter and of the repulsion range $(d_0 + 2\delta)$. This corresponds to an effective volume fraction

$$\Phi_{eff} = \Phi \left(1 + \frac{2\delta}{d_0} \right)^3.$$

Each series of data at a given ionic strength is fitted to the carnahan starling equation of state, in order to determine the value of δ (Table II). In Fig. 2, these data are plotted versus Φ_{eff}. It shows that all the data of the fluid samples can be plotted on the same curve.

Whatever $[cit]_{free}$ in this regime, the repulsion range is much longer than expected since it roughly corresponds to the Debye length of a 1:1 electrolyte with a concentration equal to that of citrate (3:1 electrolyte). This confirms the special behavior of $Na_3[cit]$, the addition of which has been shown to be nearly equivalent to NaCl addition from the point of view of phase separation in such systems [38]. This can result from finite size effects for this multivalent large ion and from counterion condensation. Note that the discrepancy between λ_{Debye} 1:1 and δ for low citrate concentrations comes from an underestimation of the screening for other reasons. Indeed, for low salt concentrations, the contribution of the noncondensed ions is no longer negligible and the real ionic strength is higher than expected according to the ionic strength imposed from the dialysis bath.

At a given volume fraction, an increase in the osmotic pressure, i.e., an increase in the repulsion range, leads to a fluid-solid transition. The threshold volume fraction of the
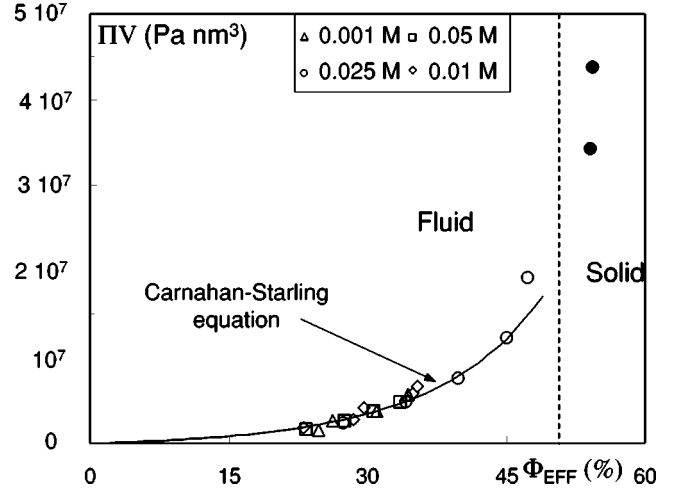

FIG. 2. The phase diagram of Fig. 1 is plotted versus effective volume fractions. The symbols are the same as in Fig. 1. The curve is the Carnahan-Starling equation of state. The dotted line corresponds to the experimental limit between the fluid and the solid phases.

transition is strongly salt dependent. Converting this threshold into an effective volume fraction taking into account the repulsion range shows that the transition occurs at a constant effective volume fraction Φ_{eff} of 50%. In Fig. 2, only the solids close to the transition line have been plotted because an effective volume fraction can no longer be defined in the same way for concentrated solids. (The repulsion ranges of two particles overlap and Φ_{eff} becomes larger than 100%). The value $\Phi_{eff} = 50\%$ determined for the fluid-solid transitions is the volume fraction above which a glass phase is observed for monodisperse hard spheres [6], and it is lower than the value expected for polydisperse hard spheres ($\Phi = 58\%$, [7]). Consequently, our effective volume fraction of transition seems reasonable, however, we cannot deduce much of the deviation from the predictions. Indeed, there is an error bar on the determination of the effective volume fraction due to the size polydispersity, and due to the very high viscosity of the dispersions close to the transition, which complicates the measurements of the volume fraction.

B. Structure of the suspensions

The structure factors of fluid and solid suspensions are determined by small-angle scattering (SANS or SAXS depending on the samples, Figs. 3 and 4). The structure factor of the fluid suspension in the low ionic strength regime exhibits a pronounced correlation peak (Fig. 3). The maximum q_{max} of this correlation peak is related to the most probable interparticle distance d_{mp} by $d_{mp} = 2\pi/q_{max}$. d_{mp} is equal to the mean interparticle distance d_{mean}, $d_{mean}^3 = V_p/\Phi$, where V_p is the particle volume (see inset of Fig. 3). The particles are thus homogeneously dispersed for this high repulsive regime [see scheme of Fig. 6(b)]. This is consistent with the very weak compressibility, which can be calculated from $S(q)_{q \to 0}$ through $(\delta\Pi/kT\delta\rho)_T = 1/S(0)$, which indicates that interactions are mainly dominated by strong long-range repulsions. The structure factor of the solid phase at low
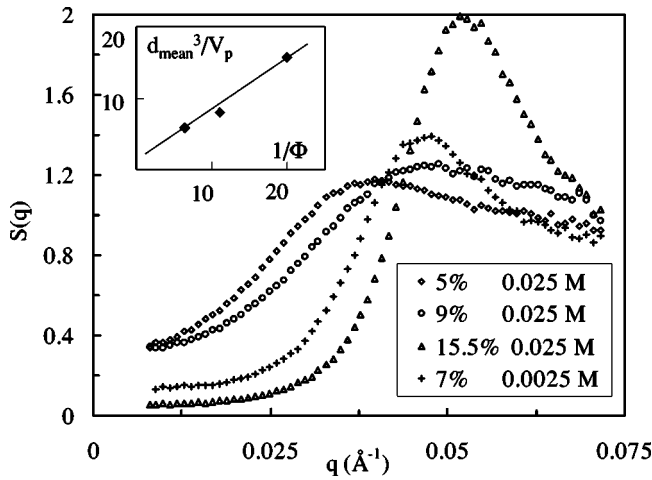
FIG. 3. Structure factors of fluid samples at low ionic strength, for sample FF5, except the crosses, that correspond to FF3. Volume fractions and citrate concentrations are given in the legend. The inset presents d_{mean}^3/V_p versus $1/\Phi$ for the three volume fractions of FF5.

ionic strength corresponds to an amorphous structure (Fig. 4): it is thus a repulsive Wigner glass. Two reasons explain the nonformation of a colloidal crystal.

(i) The preparation of the samples through osmotic compression may force the system to reach an osmotic pressure without exploring all the phase space.

(ii) The remaining polydispersity of the suspensions reduces the phase diagram zone where the formation of a crystal is allowed.

C. Interparticle potential

Figure 5 presents the estimated calculation of the interparticle potential for two particles sizes ($d_0 = 6$ nm and $d_0 = 9$ nm, which corresponds to the highest and smallest size of the study) in the repulsive regime ($[cit]_{free} = 0.01$ mol/L). For suspensions under consideration in the paper, the magnetic coupling is of the order of 1 [34] and
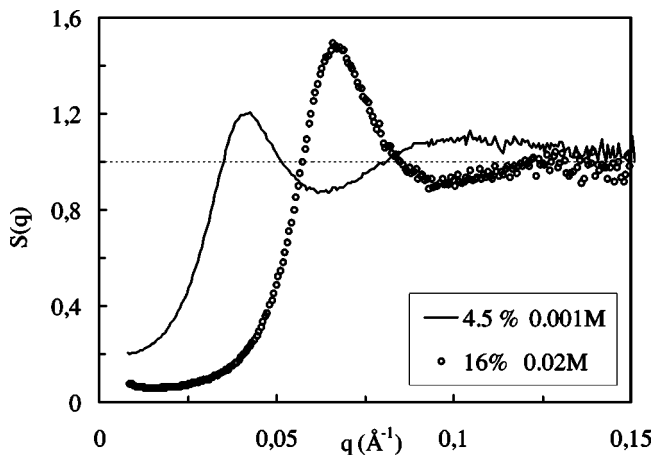

FIG. 4. Structure factors of solid samples at low citrate concentrations for FF3. Volume fractions and ionic strength are given in the legend.
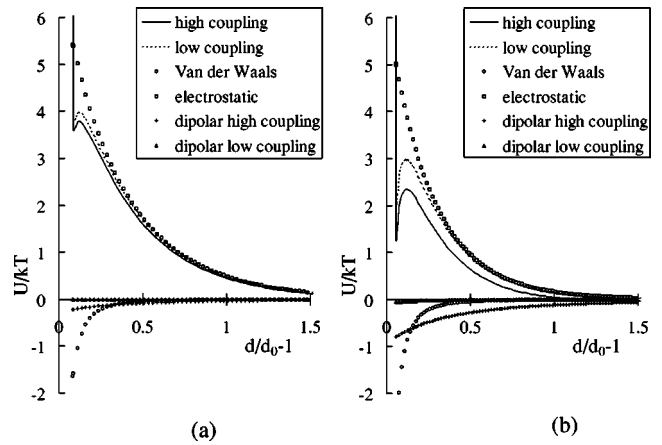

FIG. 5. Estimated calculations for the interparticle potentials at low ionic strength ($[cit]_{free} = 0.01$ mol/L). (a) $d_0 = 6$ nm and (b) $d_0 = 9$ nm.

dipolar interactions lie between the two γ limits presented in Sec. I. The potentials corresponding to these two limits are presented in Fig. 5. They are shown as functions of $d/d_0 - 1$ as this allows to easily compare the strength of attractive anisotropic dipolar attractions and attractive isotropic van der Waals attractions for particles of different sizes. There is a cutoff in the potential at $d/d_0 - 1 = 0.1$, which corresponds to the hard-core repulsion of the citrate layer.

The interparticle potential is close to a repulsive Yukawa potential for the two sizes of particles, which is in accordance with structure results. Although the dipolar interactions are much stronger for particles with $d_0 = 9$ nm than for particles with $d_0 = 6$ nm, the resulting repulsive potential is only slightly lower for the biggest particles. Note that the range of this repulsive potential is of the order of the particle size. Without an applied magnetic field, the suspensions have the phase behavior of most electrostatically stabilized systems. The isotropic electrostatic interaction can be monitored over a large range by varying the ionic strength of the suspensions. The specificity of the system is the consequence of magnetic interactions, which can be considered here as variable anisotropic pertubations.

IV. FROM REPULSIVE TO ATTRACTIVE REGIME

A. Equation of state

An addition of salt in case of a given volume fraction induces a decrease of the pressure Π, i.e., it corresponds to descending along a vertical line in the diagram of Fig. 1. This allows to cross the $A_2 = 0$ line that separates the repulsive regime from the attractive one. Such experiments show that the pressure of the suspensions with $[cit]_{free} = 0.1$ mol/L is close to the line $A_2 = 0$, as shown in Figs. 1 and 8, which feature the two phase diagrams (low I and high I).

B. Structure of the suspensions

Figure 6 shows the evolution of the structure factor with increasing ionic strength. For low I, the structure factor appears to be independent of the exact value of the ionic
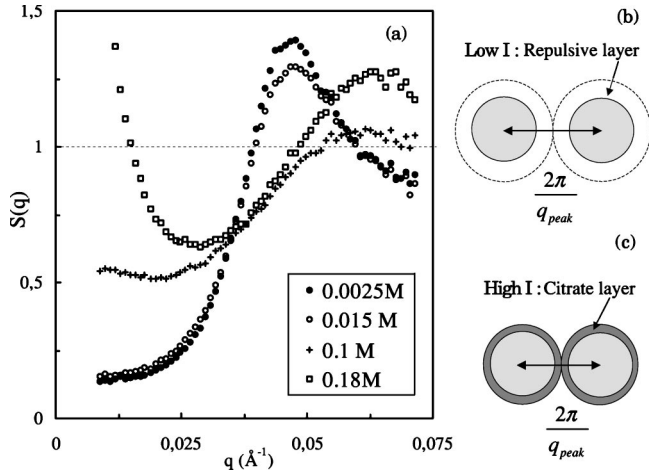
FIG. 6. (a) Evolution of the structure factor while increasing the citrate concentration. The data correspond to sample FF2 with $\Phi = 7\%$, except the empty squares that correspond to sample FF5 with $\Phi = 9\%$. The meaning of the peak is schematized for low I and high I in graphs (b) and (c).

strength. The repulsion is strong enough for the particles to be homogeneously dispersed and the correlation peak corresponds to the mean particle distance [see Fig. 6(b)]. For a citrate concentration of 0.1 mol/L, the compressibility increases and the peak is shifted toward higher q values, which now corresponds to a mean probable distance smaller than the mean distance. Interactions are still globally repulsive ($A_2 > 0$) but there are more fluctuations. For higher I ($[cit]_{free} = 0.18$ mol/L in the figure), the peak corresponds to the distance of contact between two particles [Fig. 6(c)], as in a system of hard spheres.

C. Interparticle potential

There is thus a crossover from a regime in which the particles are homogeneously dispersed due to high repulsion toward a regime in which particles can deviate significantly from their mean position because the potential becomes attractive for short ranges (Lennard-Jones like potential). This is illustrated in Fig. 7 that presents the estimated calculations for the interparticle potential for two particles sizes ($d_0 = 6$ nm and $d_0 = 9$ nm) for an ionic strength corresponding to an A_2 close to 0 ($[cit]_{free} = 0.1$ mol/L). The potential is still slightly repulsive for the smallest particles but it becomes attractive for the biggest.

A key point is the increase of the potential range due to the dipolar interactions. In Fig. 7(b), the range of the potential in the low coupling regime, which is close to the range of a pure van der Waals regime (attractions at contact), is largely increased in the high coupling regime and becomes of the order of the diameter of the particle. The behavior of this electrostatically stabilized system considered here is then similar to the behavior of the same system sterically stabilized in which the attractions range can be monitored [8–10].

V. HIGH IONIC STRENGTH REGIME

A. Equation of state

The addition of a large amount of salt changes the phase behavior of the suspension and leads to a regime in which
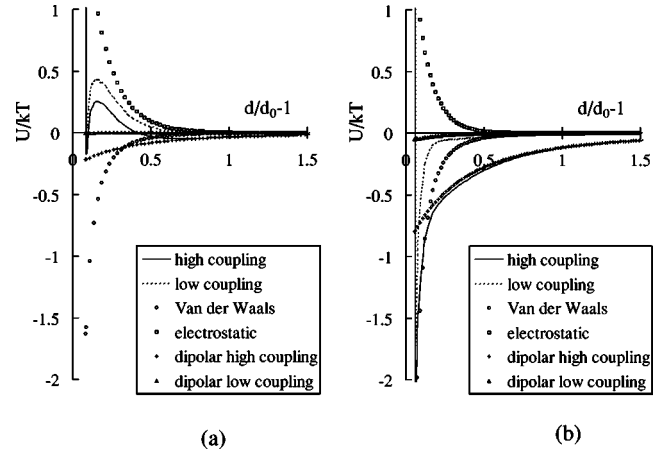

FIG. 7. Estimated calculations for the interparticle potentials at intermediate ionic strength ($[cit]_{free} = 0.1$ mol/L). (a) $d_0 = 6$ nm and (b) $d_0 = 9$ nm.

interactions are on an average attractive whatever the volume fraction (Fig. 8). The osmotic pressure of all samples in this ionic strength regime is located below the $A_2 = 0$ transition line.

Starting from a homogeneous fluid, it then becomes possible, for low enough volume fractions, to induce "gas-liquid-like" transitions, i.e., coexistence of a dense fluid phase (the liquid) with a diluted fluid phase (the gas), by addition of salt or temperature decrease. These transitions have been studied elsewhere [45] with a special focus on the critical area of the coexistence curve [46]. The coexistence line of Fig. 8 results from all these previous experiments. This method allows obtaining the liquid phase: once $\Phi > \Phi_{critical\ point}$ is reached for $\Pi > \Pi_{critical\ point}$, Π is de-
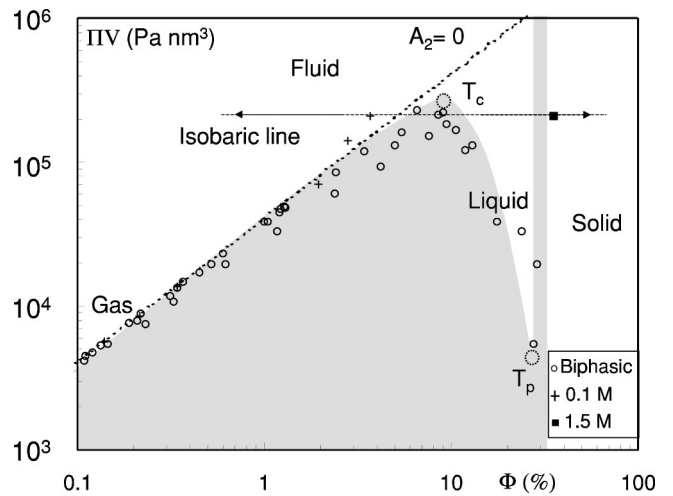

FIG. 8. Phase diagram at high ionic strength for sample FF1. The circles titled biphasic correspond to the coexistence line of the gas-liquid transition. The dashed line corresponds to $A_2 = 0$. The horizontal line is an isobaric line with $\Pi = 750$ Pa for sample FF4. The gray part of the diagram represents the biphasic areas of the theoretical phase diagram expected for an isotropic attractive interactions regime. $[cit]_{free}$ is given in the caption for the different points corresponding to monophasic samples.

TABLE III. Observations while increasing salt along an isobaric line at $\Pi = 750$ Pa. F-fluid, G-gas, L-liquid, S-solid.

[cit] (mol/L)	<0.3	0.6	1	1.5	2
Observation	F or G	G-L	G-L	S	S

creased to the vicinity of the coexistence curve of the gas-liquid transition, in the liquid area. For higher volume fractions, solid phases can be obtained.

All these transitions can be explored along isobaric lines, i.e., a series of osmotic compressions at a constant osmotic pressure $\Pi_{isobaric}$: Φ increases with increasing ionic strength. The results obtained with $\Pi = 750$ Pa are given in Table III, and this isobaric line is plotted in Fig. 8. This line corresponds to $\Pi_{isobaric} < \Pi_{critical\ point}$. At low enough volume fraction, the fluid is homogeneous, and it is possible to induce gas-liquid-like transitions while increasing ionic strength. For the highest volume fractions, solid phases can be obtained. The solid samples correspond to high ionic strengths ($>1.5M$) and high Φ (around 30% of γ-Fe_2O_3, which corresponds to 42% including the citrate shell). The liquid is not observed along this line because the range of ionic strength in which it exists is too narrow.

Along the isobaric line, the increase of Φ with ionic strength gives an indication of the screening of interactions by salt: when interactions are fully screened, the salt has nearly no influence on the volume fraction (Fig. 9).

Whatever the ionic strength, all phase transitions are reversible up to $[cit]_{free} = 2$ mol/L (maximum of solubility). The irreversible flocculation of the sample is avoided by the steric hinderence of the citrate ions adsorbed on the surface of the particles.

B. Structure of the suspensions

The structure of the samples in this high ionic strength regime is deduced from the measured structure factors (Figs. 10 and 11). Close to the destabilization thresholds, the structure factor of all samples except solids resembles the curves plotted in Fig. 10. There is a divergence of $S(q)$ at low q,

FIG. 10. Structure factor of sample FF5 at high ionic strength and several volume fractions given in the legend. The citrate concentration is 0.18 mol/L. Note that $\Phi = 15.5\%$ corresponds to a liquid phase, $\Phi = 9\%$ to a fluid phase, and $\Phi = 5\%$ to a gas phase.

which shows that the compressibility is high. The mean probable distance associated with the peak corresponds to the contact distance between particles including the citrate shell surrounding particles, and thus becomes independent of the volume fraction. The sample with $\Phi = 5\%$ corresponds to a gas phase whereas the sample with $\Phi = 15.5\%$ corresponds to a liquid phase. The sample with $\Phi = 9\%$ being above the critical point corresponds to a fluid phase.

The solid phase is still glassy as can be seen in Fig. 11. There is an upturn of $S(q)$ at low q for the solid phase. This corresponds to a large compressibility and to large density fluctuations in the system. Moreover, the mean probable distance calculated from the correlation peak corresponds to the contact of two particles.

C. Interparticle potential

Figure 12 shows the estimated calculations for the interparticle potential for two particles sizes ($d_0 = 6$ nm and d_0
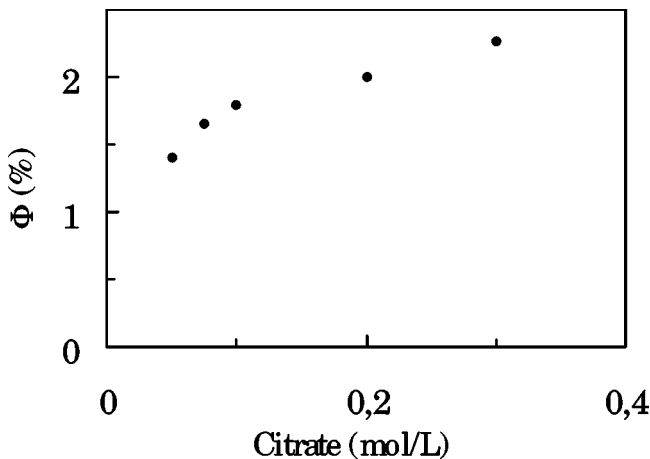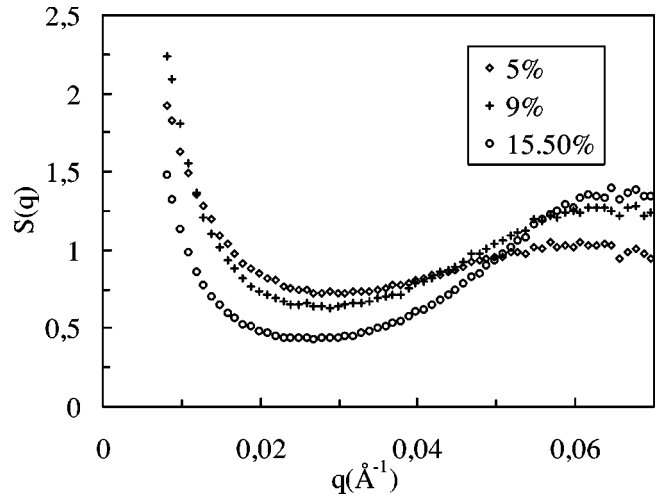

FIG. 9. Measurement of the volume fraction versus the citrate concentration along an isobaric line $\Pi = 750$ Pa for sample FF4.
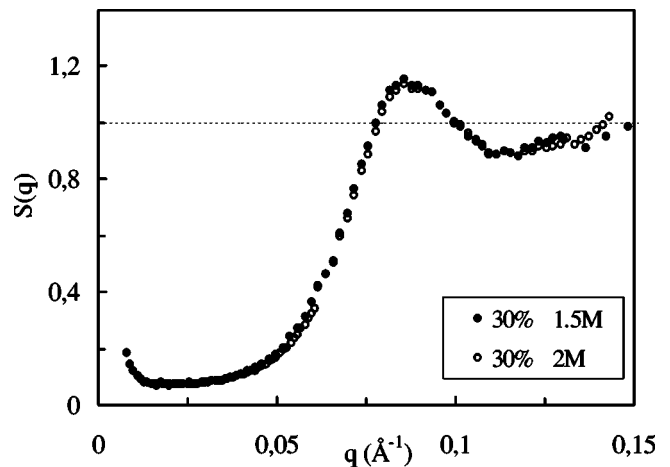

FIG. 11. Structure factor of sample FF4 at high ionic strength along the isobaric line $\Pi = 750$ Pa.
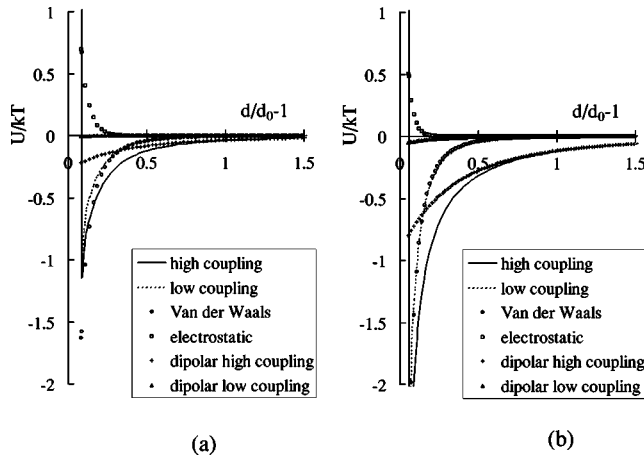
FIG. 12. Estimated calculations for the interparticle potentials at high ionic strength ($[\mathrm{cit}]_{free}=1$ mol/L). (a) $d_0=6$ nm and (b) $d_0=9$ nm.

$=9$ nm) at high ionic strength ($[\mathrm{cit}]_{free}=1$ mol/L). The long-range repulsive part that was dominating in the low ionic strength regime is lowered. The repulsive part of the potential becomes purely hard core and the attractions dominate. However, depending on the precise conditions, the system remains sensitive to a change in ionic strength. Studying the gas-liquid transition shows a shift in the threshold temperature as ionic strength changes: $\Delta T=k\Delta[\mathrm{cit}]_{free}$, with $k=1000$ K mol according to measurements in Ref. [46]. The increase of salt does not change the global shape of the interparticle potential, but changes the intensity of the attractive part [compare Figs. 7(b) and 12(b)]. It thus allows us to monitor the balance of attractions and repulsions in this domain of global attractive potential. On the contrary, in the low pressure area in which solids are obtained, the electrostatic repulsion is totally screened by the very large $[\mathrm{cit}]_{free}$ and the $S(q)$ curves are superimposed (Fig. 11 where $[\mathrm{cit}]_{free}>1.5M)$), i.e., the potential does not change anymore.

In this high ionic strength regime, we show that gas-liquid-like transitions can be observed in a colloidal suspension which is electrostatically stabilized. The existence of the liquid phase is due to the shape of the potential that is dominated by attractions. This is in agreement with predictions [2]. As we do not observe the formation of particle chains (the weight of the scattering objects is constant while in-creasing salt concentration [45]), this means that the anisotropy of the dipolar interactions do no play a part in the behavior of the systems. But, as their form is between $1/r^6$ and $1/r^3$, they increase the range of attractions compared to pure van der Waals attractions.

CONCLUSION

In summary, our results show that the experimental system presented here provides a versatile system for the study of the influence of the potential shape on the phase behavior of colloidal suspensions. This stems from the existence of both magnetic dipolar interactions and electrostatic repulsion. Experimentally, the behavior is explored by fixing the ionic strength and the volume fraction Φ through osmotic compression. The experiments demonstrate that the nature of the observed phase diagram is controlled by the ratio of attractive to repulsive interactions as predicted for colloidal suspensions [2]. If $A_2\gg0$, i.e., the repulsion dominates, only fluid-solid phases exist. If $A_2\ll0$, i.e., the attractions are strong, a phase diagram with gas, liquid, and solid phases as in atomic systems is obtained; a liquid phase and a critical area exist. This is the first colloidal suspension that allows observing a critical point associated with gas-liquid transitions and allows obtaining magnetic colloidal glasses (the solid phase). Without an applied magnetic field, the systems belong to the class of low dipolar fluids: no chaining of the particles is observed because magnetic dipolar interactions are weak enough compared to the other attractions [31].

The knowledge of this phase diagram without an applied magnetic field H allows controlling the initial state of the system before applying a field [47]. As the influence of the magnetic field H depends on the balance of the different interactions, this allows tuning the effects of an applied H for a wide range of Π and Φ values. Such effects of a magnetic field on the different phases identified in the phase diagram will be studied in a forthcoming paper.

[1] P. Pusey, in *Colloidal Suspensions in Liquids, Freezing and Glass Transitions*, Proceedings of the Les Houches Summer School, Session LI, edited by J-P. Hansen, D. Levesque, and J. Zinn-Justin (North-Holland, Amsterdam, 1991), Vol. 11, Pt. II, pp. 765–837.

[2] C.F. Tejero, A. Daanoun, H.N.W. Lekkerkerker, and M. Baus, Phys. Rev. Lett. **73**, 752 (1994).

[3] S. Hachichu, Y. Kobayashi, and A. Kose, J. Colloid Interface Sci. **42**, 342 (1973).

[4] Y. Monovoukas and A.P. Gast, J. Colloid Interface Sci. **128**, 533 (1989).

[5] E.B. Sirota, H.D. Ou-Yang, S.K. Sinha, and P.M. Chaikin, Phys. Rev. Lett. **62**, 1524 (1989).

[6] P.N. Pusey and W. Van Megen, Nature (London) **320**, 340 (1986).

[7] P. Bartlett, J. Chem. Phys. **107**, 188 (1997).

[8] A.P. Gast, C.K. Hall, and W.B. Russel, J. Colloid Interface Sci. **96**, 251 (1983).

[9] B. Vincent, J. Edwards, S. Emmett, and R. Croot, Colloids Surf. **31**, 267 (1988).

[10] H.N.W. Lekkerkerker, W.C.K. Poon, P.N. Pusey, A. Stroobants, and P.B. Warren, Europhys. Lett. **20**, 559 (1992).

[11] S.M. Ilett, A. Orrock, W.C.K. Poon, and P.N. Pusey, Phys. Rev. E **51**, 1344 (1995).

[12] A.P. Gast, C.K. Hall, and W.B. Russel, J. Colloid Interface Sci. **109**, 161 (1986).

[13] P.R. Sperry, J. Colloid Interface Sci. **99**, 1 (1984).

[14] J.E. Seebergh and J.C. Berg, Langmuir **10**, 454 (1994).

[15] J.W. Jansen, C.G. de Kruif, and A. Vrij, J. Colloid Interface Sci. **114**, 471 (1986).

[16] J.W. Jansen, C.G. de Kruif, and A. Vrij, J. Colloid Interface Sci. **114**, 481 (1986).

[17] M.H.G. Duits, R.P. May, A. Vrij, and C.G. de Kruif, Langmuir **7**, 62 (1991).

[18] J.M. Victor and J.P. Hansen, J. Chem. Soc., Faraday Trans. 1 **81**, 43 (1985).

[19] P.G. de Gennes and P.A. Pincus, Phys. Kondens. Mater. **11**, 189 (1970).

[20] K. Sano and M. Doi, J. Phys. Soc. Jpn. **52**, 2810 (1983).

[21] D. Levesque and J.J. Weis, Phys. Rev. E **49**, 5131 (1994).

[22] M.J. Stevens and G.S. Grest, Phys. Rev. Lett. **72**, 3686 (1994).

[23] V. Russier, J. Colloid Interface Sci. **174**, 166 (1995).

[24] B. Groh and S. Dietrich, Phys. Rev. E **54**, 1687 (1996).

[25] M.E. van Leeuwen and B. Smit, Phys. Rev. Lett. **71**, 3991 (1993).

[26] M.J. Stevens and G.S. Grest, Phys. Rev. E **51**, 5976 (1995).

[27] T. Tlusty and S.A. Safran, Science **290**, 1328 (2000).

[28] P.J. Camp, J.C. Shelley, and G.N. Patey, Phys. Rev. Lett. **84**, 115 (2000).

[29] J.C. Shelley, G.N. Patey, D. Levesque, and J.J. Weis, Phys. Rev. E **59**, 3065 (1999).

[30] A.F. Pshenichnikov and V.V. Mekhonoshin, JETP Lett. **72**, 182 (2000).

[31] P.I.C. Teixeira, J.M. Tavares, and M.M. Telo da Gama, J. Phys.: Condens. Matter **12**, R411 (2000).

[32] J. Israelachvili, *Van der Waals Forces between Surfaces, Intermolecular and Surface Forces* (Academic Press, New York, 1992), Chap. 11.

[33] E. Ruckenstein, Colloids Surf. **69**, 271 (1993).

[34] F. Gazeau, F. Boué, E. Dubois, and R. Perzynski, J. Phys.: Condens. Matter **15**, S1305 (2003).

[35] B.V. Derjaguin and L. Landau, Acta Physicochim. URSS **14**, 633 (1941).

[36] E.J.W. Verwey and J.T.G. Overbeek, *Theory of the Stability of Lyophobic Colloids* (Elsevier, Amsterdam, 1948).

[37] L. Belloni, in *Neutron, X-Ray and Light Scattering*, North-Holland Delta Series (North-Holland, Elsevier Science, Amsterdam, 1991), p. 135.

[38] E. Dubois, F. Boué, V. Cabuil, and R. Perzynski, J. Chem. Phys. **111**, 7147 (1999).

[39] R. Massart, IEEE Trans. Magn. **17**, 1247 (1981).

[40] R. Massart, E. Dubois, V. Cabuil, and E. Hasmonay, J. Magn. Magn. Mater. **149**, 1 (1995).

[41] *Magnetic Fluids and Applications Handbook*, edited by B.M. Berkovski, UNESCO, Series of Learning Materials/Wallingford (Begell House Inc., Wallingford, NY, 1996).

[42] V.A. Parsegian, N. Fuller, and R.P. Rand, Proc. Natl. Acad. Sci. U.S.A. **76**, 2750 (1979).

[43] F. Cousin and V. Cabuil, J. Mol. Liq. **83**, 203 (1999).

[44] J. P. Hansen and I. R. Mac Donald, *Theory of Simple Liquids* (Academic, New York, 1992).

[45] E. Dubois, R. Perzynski, F. Boué, and V. Cabuil, Langmuir **16**, 5617 (2000).

[46] F. Cousin, E. Dubois, and V. Cabuil, J. Chem. Phys. **115**, 6051 (2001).

[47] F. Gazeau, E. Dubois, F. Boué, and R. Perzynski, Phys. Rev. E **65**, 031403 (2002).